

# Context-Aware Semantic Segmentation via Stage-Wise Attention

Antoine Carreau<sup>1,2</sup> Elias Naha<sup>1,2</sup> Arthur Chansel<sup>1,2</sup> Nina Lahellec<sup>1,2</sup>  
 Jan Skaloud<sup>1</sup> Adrien Gressin<sup>2</sup>

<sup>1</sup>ESO lab. EPFL, 1015 Lausanne, Switzerland - (firstname.lastnamename)@epfl.ch

<sup>2</sup>University of Applied Sciences Western Switzerland (HES-SO / HEIG-VD),  
 Yverdon-les-Bains, Switzerland - (firstname.lastnamename)@heig-vd.ch

## Abstract

*Semantic ultra high resolution image (UHR) segmentation is essential in remote sensing applications such as aerial mapping and environmental monitoring. Transformer-based models struggle in this setting because memory grows quadratically with token count, constraining either the contextual scope or the spatial resolution. We introduce **CASWiT** (Context-Aware Stage-Wise Transformer), a dual-branch, Swin-based architecture that injects global cues into fine-grained UHR features. A context encoder processes a downsampled neighborhood to capture long-range dependencies, while a high resolution encoder extracts detailed features from UHR patches. A cross-scale fusion module, combining cross-attention and gated feature injection, enriches high-resolution tokens with context. Beyond architecture, we propose a SimMIM-style pretraining. We mask 75% of the high-resolution image tokens and the low-resolution center region that spatially corresponds to the UHR patch, then train the shared dual-encoder with small decoder to reconstruct the UHR initial image. Extensive experiments on the large-scale IGN FLAIR-HUB aerial dataset demonstrate the effectiveness of CASWiT. Our method achieves 65.83% mIoU, outperforming RGB baselines by 1.78 points. On URUR, CASWiT achieves 49.1% mIoU, surpassing the current SoTA by +0.9% under the official evaluation protocol. All codes are provided on: <https://huggingface.co/collections/heig-vd-geo/caswit>.*

## 1. Introduction

Semantic segmentation of remote sensing imagery is fundamental to many key geospatial applications, including land-use mapping, environmental monitoring, and disaster response. As these applications become more reliant on ultra-high-resolution (UHR) aerial imagery for capturing fine spatial details, it is crucial that the methods employed preserve local structures while also considering broader spatial

contexts.

Transformer-based architectures [7, 10, 28, 42] have advanced state-of-the-art results in vision tasks. However, their application to ultra-high-resolution (UHR) inputs is limited by their quadratic complexity and GPU memory constraints. Common workarounds, such as downsampling or tiling, either truncate the context necessary for interpreting complex scenes, or result in a loss of high resolution, impairing segmentation at both the object and scene levels. Recent UHR approaches therefore combine high-resolution patch processing with explicit context modeling via multi-branch or cross-scale designs [2, 20, 34], emphasizing the importance of global context and the consequences of its loss.

**Our approach.** **CASWiT**, a dual-branch hierarchical transformer, is introduced for RGB-only UHR segmentation. One branch processes high-resolution (HR) crops in order to preserve high resolution, boundaries and small objects, while a second branch ingests wider low-resolution (LR) patches in order to encode global context. These two streams interact at multiple encoder stages through compact global cross-attention blocks (HR queries over LR keys/values), enabling early context injection while remaining compute-efficient. This approach introduces context early on while keeping the computation efficient. To further improve cross-scale learning, masked image modeling (SimMIM-style [46]) is adapted to the dual-stream setting and pre-trained using large amounts of unlabelled orthophotos.

**Benchmarks.** The primary evaluation is conducted on FLAIR-HUB [13] using an RGB-only UHR protocol that leverages its geospatial structure: although FLAIR-HUB was not originally designed for UHR segmentation (it targets multi-modal/time-series Earth Observation), its georeferenced orthophotos can be reassembled into large, contiguous tiles that preserve long-range spatial context and enable UHR evaluation. Compared with URUR [21], FLAIR-HUB

offers a substantially larger scale and more carefully curated annotations (see § 4.1), making it a more effective testbed for cross-scale learning. For continuity with prior work, we also report results on **URUR**. Finally, while multi-modal inputs can boost performance on FLAIR-HUB [13, 23], we emphasize that RGB-only UHR segmentation remains a fundamental and practically relevant challenge in Earth Observation.

### Contributions.

- We introduce **CASWiT** (Context-Aware Stage-Wise Transformer), a dual-branch architecture that performs stage-wise cross-attention from HR to LR features, allowing context to be injected early in the encoding hierarchy, while preserving fine-grained details from the HR branch.
- We design a **dual-stream SimMIM** pretraining strategy that strengthens cross-scale learning and demonstrates effective transfer to large-scale UHR segmentation tasks.
- We establish an **RGB-only UHR evaluation protocol on FLAIR-HUB**, exploiting its geospatial structure to reconstruct large contiguous tiles. CASWiT consistently improves over prior RGB-only state-of-the-arts on FLAIR-HUB-RGB and URUR; all code, pretrained weights, and evaluation scripts will be released for reproducibility.

## 2. Related Work

**Dual-stream UHR segmentation.** Processing ultra-high-resolution (UHR) imagery for semantic segmentation typically requires preserving fine details while aggregating long-range context. A widely adopted strategy is to treat UHR segmentation as a *dual-stream* fusion problem: an HR stream for local structures and a complementary LR/context stream for scene-level semantics. GLNet [5] popularized this formulation with CNN backbones and late fusion by concatenation. Subsequent methods refine this template along architecture and fusion axes. WSDNet [21] integrates multi-level discrete wavelet transforms (DWT) into the UHR stream and introduces a Wavelet Smooth Loss to preserve structured context and fine textures while reducing computation, rather than relying on a single downsampled global stream with late fusion. FCtL [33] fuses features extracted at three cropping scales (CNN-based) via mid-level integration. GPWFormer [20] mixes CNNs and transformers in a dual-branch design with late fusion, while SGNet [40] introduces attention-based feature extractors in both branches prior to concatenation. STUNet [18] embeds a Transformer (specifically the Swin Transformer) and a CNN in parallel encoders and then uses a relational aggregation module to integrate global and local features hierarchically. More recently, DESformer [26] further explores dual-encoder architectures combining transformer and CNN branches for enhanced feature interaction.

Beyond these, several families target complementary aspects of UHR efficiency and accuracy.

(i) *Iterative/local patching with global guidance*: GLNet’s original strategy inspired follow-ups that iteratively process UHR patches under LR guidance. (ii) *Proposal/selection to reduce UHR cost*: PPN [22, 44] allocates compute to informative regions only. (iii) *Shallow all-pixel models*: ISDNet [14], WSDNet [21], GPWFormer [20], and SGHRQ [24] aim to process full UHR images with reduced complexity to avoid iterative patching, often correcting HR predictions using LR-derived context. Recent memory-efficient approaches like WCTNet [3], EFFNet [36], and RingFormer-Seg [48] tackle the memory-accuracy tradeoff through token filtering, global-local branches, and efficient fusion strategies.

(iv) *Boundary refinement/ensemble*: CascadePSP [8], MagNet [19], and FCtL [33] emphasize progressive refinement and multi-scale ensembling to fix boundary errors. Most of these approaches rely on mid/late fusion, where HR and LR features interact after substantial single-stream processing, whereas early fusion can be beneficial when both inputs share similar representational spaces [1].

**Single-stream HR backbones.** An alternative to dual-stream fusion is to rely on hierarchical vision transformers or multi-scale CNNs that capture locality and globality within a single stream. Representative examples include Swin Transformer [28, 29] and PVT [41, 42], alongside UHR-oriented single-stream variants [15, 27, 35, 37, 43, 47]. While these models improve scalability compared to vanilla ViT, balancing spatial resolution and memory for truly UHR inputs remains challenging.

**Fusion mechanisms and module placement.** Despite the intuitive complementarity of HR and LR signals, many dual-stream models still perform simple mid/late fusion (concatenation/summation). Attention-based alignment between heterogeneous resolutions is less explored at *multiple* depths, even though cross-attention provides a systematic mechanism to condition HR features on LR context (and vice versa) early enough to guide subsequent hierarchy building. Works like DESformer [26] introduces a mid-level, multi-depth Feature Interaction Module that fuses CNN and Transformer features inside the encoder. A more complex mechanism like CTCFNet [30] uses a CNN–Transformer backbone and fuses local and global features at the same scale via a mid-to-late Feature Aggregation Module and a bi-directional decoder. This landscape motivates designs that : (a) adopt stronger backbones than shallow CNNs for at least one stream, and (b) enable lightweight, stage-wise cross-attention to inject context into HR processing before irreversible locality is set.

### Most recent advances: Resolution-Biased Uncertainty.

This recent work [34] revisits the dual-stream paradigm with an explicit estimator of resolution-biased uncertainties in the LR stream, using them to guide HR/LR interaction. Compared to selection-based methods (e.g., PPN) and all-pixel models (e.g., ISDNet, WSDNet), it shows that modeling where LR cues are reliable can further improve dual-stream effectiveness without heavy iterative costs.

**Other UHR dense prediction tasks.** Similar mechanisms have been explored in other dense UHR tasks such as salient object detection or monocular depth estimation, where dual-stream designs, patch selection, and uncertainty estimation also play key roles [14, 25, 32, 38, 39, 44].

**Positioning of our approach.** Building on these insights, CASWiT adopts the dual-stream line but differs in two key aspects. First, both streams use modern hierarchical transformers, strengthening representation quality relative to conventional CNN backbones. Second, we insert lightweight cross-attention from the very first encoder stages to learn cross-scale representations across the hierarchy, rather than restricting fusion to mid/late depths. Complementary to uncertainty-driven guidance [34], CASWiT focuses on where and when to fuse via cross-attention (early-to-mid), showing consistent gains on RGB-only UHR evaluation. We further couple this design with a SimMIM-style [46] pretraining tailored to aerial orthophotos to initialize context-aware features for UHR scenes.

## 3. Method

CASWiT (Context-Aware Stage-Wise Transformer) is a dual-branch architecture that fuses high-resolution (HR) features with low-resolution (LR) contextual features through compact cross-attention blocks inserted after each encoder stage (Fig. 1). Each block applies HR-LR cross-attention followed by a residual MLP, optionally modulated by a learned gate. The network is trained with supervision on the HR output and an auxiliary LR loss weighted by  $\alpha$ . At inference, the LR stream remains to provide context, but its decoder/head is removed.

### 3.1. Overview

CASWiT combines a HR Swin encoder [28] that preserves high resolution features with a LR Swin encoder that captures global contextual features from a larger field of view. Both encoders share identical hierarchical configurations (stages  $\{1..4\}$ , channel schedule  $C_s$ ). Cross-attention modules are inserted after each stage to inject LR context into the HR stream. The HR features are decoded by a UPerNet head to produce the final logits.

### 3.2. Dual-resolution encoder

**Inputs.** Given an HR crop  $I^{\text{HR}} \in \mathbb{R}^{H \times W \times 3}$  and a co-registered LR image  $I^{\text{LR}}$  (downsampled from a larger FoV), the two Swin encoders produce stage-wise feature maps:

$$X_s^{\text{HR}} \in \mathbb{R}^{H_s \times W_s \times C_s}, \quad X_s^{\text{LR}} \in \mathbb{R}^{\hat{H}_s \times \hat{W}_s \times C_s}.$$

The HR and LR features may differ in spatial size; they are flattened into token sequences before fusion.

**Cross-attention fusion block.** At each stage  $s$ , we perform multi-head cross-attention (MHA) from HR queries to LR keys/values:

$$\begin{aligned} Q &= \text{LN}(X_s^{\text{HR}})W_Q \\ K &= \text{LN}(X_s^{\text{LR}})W_K, \quad V = \text{LN}(X_s^{\text{LR}})W_V, \\ A_s &= \text{MHA}(Q, K, V). \end{aligned}$$

The final HR features at stage  $s$ ,  $\tilde{H}_s$  is obtained via a residual connection and an optional learned gate  $\gamma_s$ :

$$H'_s = X_s^{\text{HR}} + \gamma_s \odot A_s, \quad \tilde{H}_s = H'_s + \text{MLP}(H'_s),$$

where  $\gamma_s = \tanh(g_s)$  is a learned scalar stage-wise gate broadcast over HR tokens. The gate controls how much contextual features from the LR stream is injected into HR features. While it can improve training stability, the ungated variant slightly outperforms it; both versions are reported in § 4.

### 3.3. Decoder and prediction heads

We adopt UPerNet [45] as the HR decoder, where stage features  $\{\hat{X}_s^{\text{HR}}\}_{s=1}^4$  are fused by a Feature Pyramid Network (FPN) with a Pyramid Pooling Module (PPM) then classified by the Head. A LR decoder mirrors the same structure and is used only during training for auxiliary supervision, it is removed at inference.

### 3.4. Supervised objectives

Let  $\hat{Y}^{\text{HR}} \in \mathbb{R}^{H \times W \times K}$  and  $\hat{Y}^{\text{LR}} \in \mathbb{R}^{\hat{H} \times \hat{W} \times K}$  be the logits from the HR and LR heads, and let  $Y \in \{1, \dots, K\}^{H \times W}$  be the ground-truth labels. We compute standard pixel-wise cross-entropy on HR:

$$\mathcal{L}_{\text{HR}} = -\frac{1}{HW} \sum_p \sum_k \mathbf{1}[Y_p=k] \log \text{Softmax}(\hat{Y}_p^{\text{HR}})_k.$$

For LR supervision, we use the downsampled label map  $Y^{\downarrow} \in \{1, \dots, K\}^{\hat{H} \times \hat{W}}$  (nearest-neighbor):

$$\mathcal{L}_{\text{LR}} = -\frac{1}{\hat{H}\hat{W}} \sum_p \sum_k \mathbf{1}[Y_p^{\downarrow}=k] \log \text{Softmax}(\hat{Y}_p^{\text{LR}})_k.$$

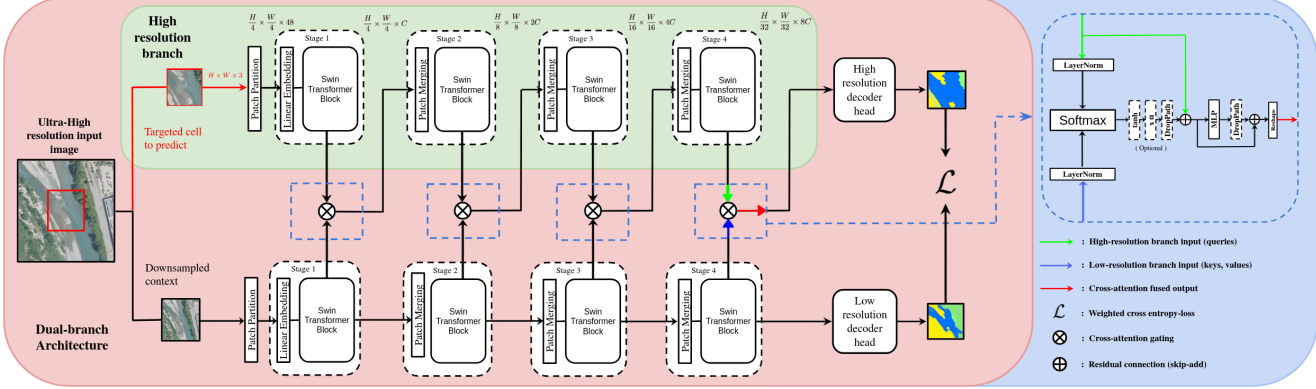


Figure 1. **Proposed architecture (CASWiT).** A dual-branch (green) encoder for ultra-high-resolution imagery: the **high-resolution (HR)** branch processes the targeted tile to predict, while the **low-resolution (LR)** branch (pink) ingests a downsampled global context. At every Swin *stage* (1→4), HR features supply queries ( $Q$ ) and LR features provide keys/values ( $K, V$ ) to a multi-scale **cross-attention** module with *gating* ( $\otimes$ ) and *residual connections* ( $\oplus$ ), enabling controlled context exchange (right panel). Two decoder heads (HR/LR) are **jointly optimized** via a **weighted cross-entropy loss** ( $\mathcal{L}$ ), injecting global LR cues while preserving HR detail. Intermediate resolutions ( $H/4 \dots H/32$ ) follow Swin patch-merging; a MLP further refines the fused output.

The total loss is the weighted sum

$$\mathcal{L} = \mathcal{L}_{\text{HR}} + \alpha \mathcal{L}_{\text{LR}},$$

where  $\alpha$  controls the contribution of the LR auxiliary head (set to 0.5 in our experiments).

### 3.5. Self-supervised pretraining (SimMIM-style)

We adapt a simple framework for masked image modeling (SimMIM) [46] to the dual-stream encoder and keep the HR-LR fusion active throughout pretraining.

**Masking strategy.** On the HR stream, we apply random masking with ratio  $r_{\text{HR}}$  (default 0.75). On the LR stream, we apply a **centered** masking with ratio  $r_{\text{LR}}$  (default 0.5) to preserve global scene layout without keeping the corresponding part of HR. In both cases, the masked tokens are replaced with a learnable mask token at the stage 1 embedding dimension (with no zeroing), as in many frameworks [17, 46]. Cross-attention therefore consumes LR features in which masked positions carry the learned mask token embedding.

**Reconstruction head and objective.** Only the HR branch is reconstructed. From the last HR stage ( $s=4$ ), we use a  $1 \times 1$  convolution producing  $3s^2$  channels followed by a PixelShuffle with stride  $s$  (equal to the total downsampling factor of the HR encoder) to map tokens back to RGB at input resolution. Let  $\hat{I}^{\text{HR}}$  be the reconstruction. We minimize a masked  $\ell_1$  loss over the masked HR pixels only:

$$\mathcal{L}_{\text{SSL}} = \frac{1}{3|M_{\text{HR}}^{\text{pix}}|} \sum_{p \in M_{\text{HR}}^{\text{pix}}} \|\hat{I}_p^{\text{HR}} - I_p^{\text{HR}}\|_1$$

where  $M_{\text{HR}}^{\text{pix}}$  is obtained by upsampling the HR *patch* mask to pixel resolution using the stage-1 patch size. During SSL, masked tokens are replaced by a learnable mask embedding; fusion remains active so the encoder can leverage LR semantics to infer missing HR content. Fig. 2 illustrates our dual-stream masking strategy, with random HR masking and centered LR masking used during self-supervised pretraining.

**Transfer.** After SSL, we discard the reconstruction head and fine-tune the dual-stream encoders with cross-attention under the supervised objective in §3.4.

## 4. Experiments

### 4.1. Datasets

**FLAIR-HUB.** We use the FLAIR-HUB dataset [13], a large-scale multimodal extension of [12], comprising 241,100 RGB patches of size  $512 \times 512$  at 0.20 m GSD, annotated into 15 classes. To enable RGB-only UHR evaluation while remaining comparable to the official per-patch setting, we construct for each HR patch a geospatially aligned  $3 \times 3$  context tile using its eight neighbors (GeoTIFF coordinates), yielding a  $1024 \times 1024$  composite that we downsample by 2 to obtain a  $512 \times 512$  LR input co-registered with the HR patch. When neighbors are missing at borders, we fill gaps with black padding to keep same dimensions for all patches. This protocol preserves long-range spatial context while keeping the input size compatible with standard backbones (see Fig. 3).

**URUR.** The URUR dataset [21] contains 3,008 UHR RGB images of size  $5120 \times 5120$  from 63 cities with 8 land-



Figure 2. Self-supervised inference results on the CASWiT architecture. Each image (left to right) shows: original high-resolution image, high-resolution image with random masking, low-resolution image with central masking, and the reconstruction of the high-resolution image after SimMIM-style pretraining.



Figure 3. HR/LR construction on FLAIR-HUB. Red: original HR patch ( $512 \times 512$ ). Green: georeferenced  $3 \times 3$  neighborhood assembled into a  $1024 \times 1024$  context, then downsampled  $\times 2$  to form the LR input ( $512 \times 512$ ).

cover classes. We follow the official split: 2,157 train, 280 val, 571 test. URUR has been influential for UHR evaluation, however, we observed occasional image–mask inconsistencies (e.g., local misalignment) that can affect evaluation metrics (see Fig. 4). We therefore report URUR results, but we advise interpreting URUR metrics with care: scores can be underestimated or display higher variance due to occasional image–mask non-conformities, and, as discussed in [34], the handling of the other class may depress IoU (near zero) because it appears sparsely.

**SWISSIMAGE (unlabeled, for SSL).** For self-supervised pretraining, we use large-scale unlabeled orthophotos from the SWISSIMAGE archive at 0.20 m GSD (total  $\sim 1067$  Gpx; excluded from supervised splits). This corpus provides over  $40 \times$  more pixels than labeled



Figure 4. URUR: illustrative annotation mismatch. Example where the provided mask (overlaid) locally diverges from the RGB content; such cases are occasional but can affect evaluation metrics. See §. 4.1 and supplementary for more examples.

training data from official test split of FLAIR-HUB, enabling robust masked reconstruction pretraining.

**Other UHR datasets.** For completeness, we note that the community frequently reports on INRIA Aerial [31] and DeepGlobe [9]. We do not include them in our main evaluation because (i) INRIA Aerial provides building–background annotations only (single-class target), which is less effective for multi-class UHR segmentation, and (ii) both datasets are significantly smaller than FLAIR-HUB and URUR, offering limited coverage for large-scale cross-scale analysis. We focus our study on FLAIR-HUB (primary, RGB-only UHR protocol) and URUR (legacy benchmark) to balance scale, class diversity, and continuity with prior work.

## 4.2. Evaluation Protocols

We report standard semantic segmentation metric, including mean Intersection-over-Union (mIoU) and mean F1 score (mF1), computed over all non-void classes. For FLAIR-HUB, we follow the official split named “split\_flairhub” and

report per-class results in the supplementary. For URUR, we follow the original train/val/test protocol with the configuration of 8 classes (with class "other" for comparison with previous work) and also report per-class results in the supplementary. Inferences are performed **without** overlapping sliding windows on FLAIR-HUB and URUR.

**Mean Boundary IoU (mBIoU).** Beyond region overlap, we evaluate boundary quality using the mean Boundary IoU metric (mBIoU) [6]. For each class  $c$ , we extract thin boundary bands from the ground truth ( $B_Y^c$ ) and the prediction ( $B_{\hat{Y}}^c$ ) by dilating their contours.

The boundary IoU for class  $c$  and mBIoU are:

$$\text{bIoU}(c) = \frac{|B_Y^c \cap B_{\hat{Y}}^c|}{|B_Y^c \cup B_{\hat{Y}}^c|}, \quad \text{mBIoU} = \frac{1}{C} \sum_{c=1}^C \text{bIoU}(c)$$

Compared to standard mIoU, mBIoU is insensitive to large homogeneous regions and focuses on how well object edges are localized.

### 4.3. Implementation Details

All experiments are implemented in PyTorch and trained on 4× NVIDIA L40S GPUs (48 GB each) using Distributed Data Parallel (DDP). We use the AdamW optimizer with an initial learning rate of  $6 \times 10^{-5}$ , decayed to  $1 \times 10^{-6}$  through a cosine annealing scheduler, and a weight decay of 0.01. Batch size is set to 20 (5 per GPU) for URUR and 16 (4 per GPU) for FLAIR-HUB. Training runs for 20 epochs with a crop size of  $512 \times 512$  for both HR and LR inputs (LR initially  $1024 \times 1024$  and subsampled to  $512 \times 512$ ). No data augmentation is applied, unless specified, to ensure a controlled comparison across methods and datasets.

For all experiments, both HR and LR branches use identical backbones, CASWiT-Base means the use of 2 Swin-Base backbones. Unless otherwise specified, the gating mechanism is disabled (see ablation in § 4.5), and the auxiliary LR supervision weight is set to  $\alpha = 0.5$ .

**Self-supervised pretraining.** We perform SimMIM-style pretraining on the unlabeled SWISSIMAGE corpus for 100 epochs before fine-tuning. Masking ratios are set to 75% for HR (random) and 50% for LR (centered), the latter designed to maintain global layout while preventing trivial pixel copying across scales. Both streams and cross-attention blocks are optimized jointly during pretraining. The pretrained weights are then used for direct fine-tuning on FLAIR-HUB and URUR without intermediate adaptation.

### 4.4. Quantitative Results

**FLAIR-HUB (RGB-only UHR protocol).** Table 1 reports RGB-only segmentation performance on the FLAIR-HUB benchmark under the proposed UHR protocol. We

Model	mIoU (%)↑	mF1 (%)↑	mBIoU (%)↑
<i>RGB Baselines (official FLAIR-HUB)</i>			
Swin-T + UPerNet [13]	62.01	75.27	-
Swin-S + UPerNet [13]	61.87	75.11	-
Swin-B + UPerNet [13]	64.05	76.88	-
→ retrained	64.02	76.64	32.57
Swin-L + UPerNet [13]	63.36	76.35	-
<i>Ours (RGB-only UHR protocol)</i>			
<b>CASWiT-Base (Ours)</b>	65.11	77.71	35.87
<b>CASWiT-Base-SSL (Ours)</b>	65.35	77.87	35.99
<b>CASWiT-Base-SSL-aug (Ours)</b>	<b>65.83</b>	<b>78.22</b>	<b>36.90</b>

Table 1. Results on the FLAIR-HUB test set under the RGB-only UHR protocol. CASWiT achieves the best RGB-only performance.

compare CASWiT to the four official Swin+UPerNet RGB baselines released by the dataset authors [13], which include the Tiny, Small, Base, and Large variants trained on RGB imagery. Our CASWiT-Base model achieves **65.11%** mIoU, outperforming all RGB counterparts. With self-supervised pretraining (CASWiT-Base-SSL), the score further improves to **65.35%** mIoU and even **65.83%** mIoU when spatial and radiometric augmentations are added during training (CASWiT-Base-SSL-aug). For reference, the best multimodal configuration reported in [23], which combines RGB, Near IR, DSM (Digital Surface Model), and Sentinel-2 time-series, reaches 65.9% mIoU; this highlights that our RGB-only results approach the global state-of-the-art despite relying solely on single-modality imagery. Beyond mIoU/mF1, CASWiT improves boundary quality: mBIoU rises from 32.57 (retrained Swin-Base) to **35.87** with CASWiT-Base (+3.30), and to **36.90** with SSL and augmentations (+4.33), consistent with the corresponding  $\Delta\text{mIoU} +1.09/ +1.81$  and  $\Delta\text{mF1} +1.07/ +1.58$ .

**URUR (legacy benchmark).** Table 2 summarizes results on URUR. CASWiT consistently surpasses prior UHR-specific architectures such as WSDNet [21], and the recent Boosting Dual-Branch model [34], reaching **48.7%** mIoU and **49.1%** mIoU with self-supervised pretraining. This improvement confirms that early, stage-wise cross-attention enhances both detail preservation and contextual reasoning in ultra-high-resolution segmentation. We emphasize that, as discussed in § 4.1, occasional annotation inconsistencies and the handling of the *other* class can cause mIoU metric to be underestimated.

### 4.5. Ablation Studies

We perform a series of ablation experiments on the FLAIR-HUB validation split to analyze the impact of the key design choices in CASWiT. Unless otherwise stated, all variants use a Swin-Base backbone and are trained under identical conditions (20 epochs, crop size  $512 \times 512$ , no data augmentation). We systematically vary the cross-attention pattern,

Model	mIoU (%)↑	Mem (MB)↓
<i>Generic Models</i>		
PSPNet [8]	32.0	5482
ResNet18 [16] + DeepLabv3+ [4]	33.1	5508
STDC [11]	42.0	7617
<i>UHR Models</i>		
GLNet [5]	41.2	3063
FCLt [33]	43.1	4508
ISDNNet [14]	45.8	4920
WSDNet [21]	46.9	4510
Boosting Dual-branch [34]	48.2	3682
<b>CASWiT-Base (Ours)</b>	<b>48.7</b>	3530
<b>CASWiT-Base-SSL (Ours)</b>	<b>49.1</b>	3530

Table 2. Experiment results on the **URUR** test set. CASWiT outperforms prior UHR-specific approaches while remaining memory-efficient.

the auxiliary LR supervision weight  $\alpha$ , the gating mechanism, and the SSL initialization. Results are summarized in Table 3.

**Cross-attention.** To isolate the effect of cross-scale fusion, we remove the LR/context branch and disable all cross-attention modules. This effectively reduces CASWiT to a standard Swin-Base encoder with a UPerNet decoder, i.e., the RGB baseline used in the FLAIR-HUB paper. On the validation set, this single-stream baseline reaches 70.11 mIoU. When enabling all-stage cross-attention without LR supervision ( $\alpha=0$ ), performance increases to 70.30 mIoU, and further rises to 71.40 mIoU once auxiliary LR supervision is added ( $\alpha=0.5$ ). This corresponds to a gain of +1.29 mIoU over the re-trained Swin-Base baseline, indicating that explicit context aware fusion is responsible of the improvement. We also verified that our Swin-Base reproduction closely matches the official FLAIR-HUB RGB results on the test set (see Sec. 4), which validates our implementation and training setup.

**Stage-wise fusion.** We compare cross-attention applied only at the first stage, only at the last stage, and at all four encoder stages. Using cross-attention exclusively at the last stage (Stage-4 only) already provides a strong improvement over the single-stream baseline (71.32 vs. 70.11 mIoU), confirming that injecting LR context at a high semantic level is beneficial. Relying on the first stage alone is less effective (69.89 mIoU), suggesting that early low-level interaction is not sufficient by itself. Our full CASWiT-Base model, which performs stage-wise fusion at all levels, achieves the best overall result (71.40 mIoU), indicating that combining early and late cross-scale interactions yields the most balanced trade-off between fine detail and global coherence.

**Auxiliary LR supervision.** We vary the auxiliary loss weight  $\alpha$  from 0 to 0.5. Comparing the all-stage variants,

Variant	Cross-Attn	$\alpha$	mIoU (%)↑	mF1 (%)↑
Baseline (no CA)	x	0.0	70.11	81.72
All-stage + gating on	(All, gated)	0.0	70.15	81.78
All-stage	(All)	0.0	70.30	81.89
Stage-1 fusion only	(Stage 1)	0.5	69.89	81.56
Last-stage fusion only	(Stage 4)	0.5	71.32	82.56
<b>CASWiT-Tiny</b>	(All)	0.5	70.91	82.24
<b>CASWiT-Base</b>	(All)	0.5	71.40	82.62
<b>CASWiT-Base-SSL</b>	(All)	0.5	71.55	82.78

Table 3. Ablation study on the **FLAIR-HUB** validation set. Each component is varied independently; "CA" denotes cross-attention,  $\alpha$  the LR supervision. All models use the Swin-Base backbone and are trained for 20 epochs without augmentation.

adding LR supervision ( $\alpha=0.5$ ) improves mIoU from 70.30 to 71.40 and also leads to smoother validation curves (not shown), suggesting that lightweight LR guidance regularizes the shared representation and facilitates optimization.

**Gating mechanism.** We evaluate the optional learned gate  $g_s$  used to scale the cross-attention residuals. With all-stage fusion and  $\alpha=0$ , enabling gating yields 70.15 mIoU, slightly below the ungated counterpart (70.30 mIoU). We did not observe consistent benefits in terms of stability or final accuracy, and we therefore keep gating disabled in our main configuration (leading a  $\gamma_s = 1$ ).

**Model size.** We additionally evaluate a lighter variant, CASWiT-Tiny, which uses the same cross-attention design but a reduced-capacity backbone. Despite its substantially smaller parameter budget, CASWiT-Tiny reaches 70.91 mIoU, only 0.49 mIoU below CASWiT-Base. This confirms that CASWiT scales gracefully and that the proposed fusion strategy remains effective even in compact configurations.

**Self-supervised pretraining.** Finally, we compare models trained from scratch to those initialized with our SimMIM-style pretraining on SWISSIMAGE. On the FLAIR-HUB validation set, pretraining increases performance from 71.40 to 71.55 mIoU (+0.15), and we observe larger gains on the test set (see Sec. 4). Qualitatively, the pretrained model produces sharper boundaries and more coherent large structures, indicating that masked reconstruction on large-scale orthoimagery exposes the network to structural cues that are beneficial for UHR semantic segmentation.

## 4.6. Qualitative Analysis

We provide qualitative visualizations to further illustrate the behavior of CASWiT across self-supervised settings.

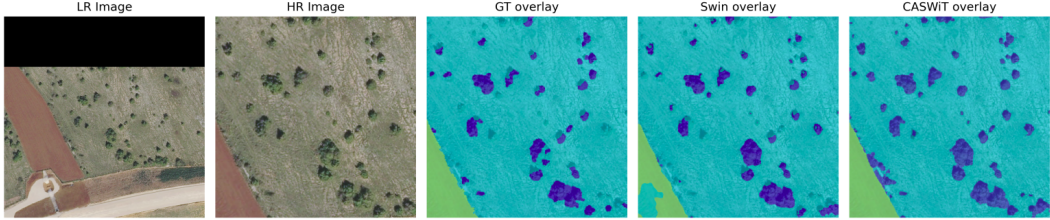


Figure 5. Qualitative comparison on IGN FLAIR-HUB. From left to right: LR image (note the missing band at the top), HR image crop, ground-truth overlay, RGB baseline (Swin-Base) overlay, and CASWiT overlay. CASWiT better recovers small vegetation patches and yields crisper boundaries, closely matching the GT while reducing false positives on bare soil and road areas (bottom-left). Despite the LR artifact (black band), CASWiT remains stable.

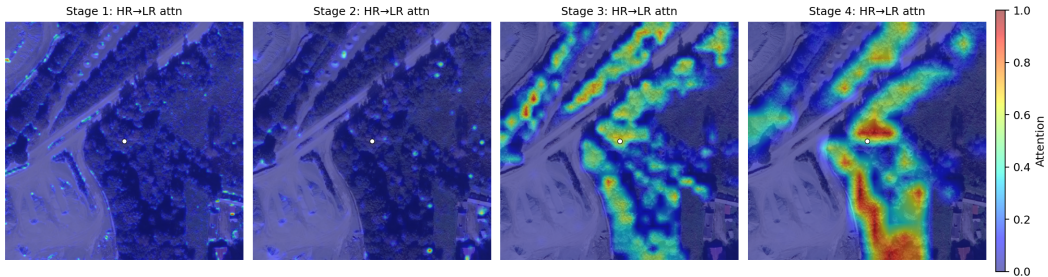


Figure 6. Cross-attention maps after SSL pretraining and supervised fine-tuning. Visualization of HR-LR cross-attention for each stage of CASWiT. The queried HR pixel is marked by a white dot; attention weights are reprojected onto the LR token grid, overlaid on the LR image.

**Segmentation results on FLAIR-HUB.** Fig. 5 shows a representative example from the FLAIR-HUB test set comparing CASWiT-Base-SSL to the RGB Swin-B baseline (more examples are provided in supplementary). Our model produces cleaner boundaries and better preserves fine structures, such as narrow roads and building outlines. It also reduces semantic bleeding between adjacent classes.

**Cross-attention visualization.** To understand how context propagates across scales, we visualize the attention maps from HR queries to LR keys at different encoder stages (Fig. 6 and more in supplementary materials). The late stages (stage 3-4) focus on the broad semantic layout, such as roads, vegetation and water bodies, while the deeper stages concentrate on the fine boundaries (stages 1-2). This progressive refinement supports the intuition that multi-stage cross-attention enables context to be injected early and consolidated hierarchically.

**Self-supervised reconstruction.** Fig. 2 illustrates the masked reconstruction process during self-supervised pre-training. Random HR masks (75%) and centered LR masks (50%) are applied jointly; the network must reconstruct missing HR pixels using both visible HR context and LR cues. CASWiT successfully recovers fine-grained textures and object geometry, indicating that the dual-stream fusion

effectively learns cross-scale correspondences.

## 5. Conclusion

### 5.1. Conclusion and Limitations

We introduced **CASWiT**, a cross-attentive dual-branch backbone for ultra-high-resolution RGB aerial segmentation that fuses HR detail with LR scene context via lightweight, stage-wise cross-attention. We also proposed an RGB-only **FLAIR-HUB-UHR** evaluation protocol that leverages geospatial structure to preserve long-range context. On this benchmark, CASWiT establishes a new RGB-only state of the art (**65.83** mIoU with SSL and augmentations) and improves the legacy URUR benchmark to **49.1** mIoU. Beyond mIoU, CASWiT increases boundary quality on FLAIR-HUB by **+4.33** mbIoU over the previous state-of-the-art RGB model. These gains stem primarily from explicit cross-scale fusion and are further reinforced by SimMIM-style pretraining on large-scale orthophotos.

### 5.2. Perspectives

Our core contribution is the backbone: CASWiT delivers stronger, context-aware features while remaining head-agnostic. A direct next step is to pair CASWiT with more powerful decoders [7] to better exploit its multi-scale representations.

## 6. Acknowledgements

We would like to thank Shanci Li for his valuable assistance with the dataset, as well as Amir Zamir and his team for their constructive feedback and insightful discussions as part of the Visual Intelligence course. This research was supported by the Canton of Vaud and the INSIT Institute at HEIG-VD.

## References

- [1] T. Baltrušaitis, C. Ahuja, and L.-P. Morency. Multimodal machine learning: A survey and taxonomy. *IEEE Transactions on Pattern Analysis and Machine Intelligence*, 41(2):423–443, 2019. [2](#)
- [2] Chun-Fu (Richard) Chen, Quanfu Fan, and Rameswar Panda. Crossvit: Cross-attention multi-scale vision transformer for image classification. In *Proceedings of the IEEE/CVF International Conference on Computer Vision (ICCV)*, pages 357–366, 2021. [1](#)
- [3] Lijia Chen, Honghui Chen, Yanqiu Xie, Tianyou He, Jing Ye, and Yushan Zheng. An efficient and light transformer-based segmentation network for remote sensing images of landscapes. *Forests*, 14(11), 2023. [2](#)
- [4] Liang-Chieh Chen, Yukun Zhu, George Papandreou, Florian Schroff, and Hartwig Adam. Encoder-decoder with atrous separable convolution for semantic image segmentation. In *Proceedings of the European Conference on Computer Vision (ECCV)*, 2018. [7](#)
- [5] Wuyang Chen, Ziyu Jiang, Zhangyang Wang, Kexin Cui, and Xiaoning Qian. Collaborative global-local networks for memory-efficient segmentation of ultra-high resolution images. In *Proceedings of the IEEE/CVF Conference on Computer Vision and Pattern Recognition (CVPR)*, 2019. [2, 7](#)
- [6] Bowen Cheng, Ross Girshick, Piotr Dollár, Alexander C. Berg, and Alexander Kirillov. Boundary iou: Improving object-centric image segmentation evaluation, 2021. [6](#)
- [7] Bowen Cheng, Ishan Misra, Alexander G. Schwing, Alexander Kirillov, and Rohit Girdhar. Masked-attention mask transformer for universal image segmentation, 2022. [1, 8](#)
- [8] Ho Kei Cheng, Jihoon Chung, Yu-Wing Tai, and Chi-Keung Tang. Cascadepsp: Toward class-agnostic and very high-resolution segmentation via global and local refinement. In *Proceedings of the IEEE/CVF Conference on Computer Vision and Pattern Recognition (CVPR)*, 2020. [2, 7](#)
- [9] Ilke Demir, Krzysztof Koperski, David Lindenbaum, Guan Pang, Jing Huang, Saikat Basu, Forest Hughes, Devis Tuia, and Ramesh Raskar. Deepglobe 2018: A challenge to parse the earth through satellite images. In *Proceedings of the IEEE Conference on Computer Vision and Pattern Recognition (CVPR) Workshops*, 2018. [5](#)
- [10] A. Dosovitskiy, L. Beyer, A. Kolesnikov, D. Weissenborn, X. Zhai, T. Unterthiner, M. Dehghani, M. Minderer, G. Heigold, S. Gelly, J. Uszkoreit, and N. Houlsby. An image is worth 16x16 words: Transformers for image recognition at scale. In *International Conference on Learning Representations*, 2021. [1](#)
- [11] Mingyuan Fan, Shenqi Lai, Junshi Huang, Xiaoming Wei, Zhenhua Chai, Junfeng Luo, and Xiaolin Wei. Rethinking bisenet for real-time semantic segmentation. In *Proceedings of the IEEE/CVF Conference on Computer Vision and Pattern Recognition (CVPR)*, pages 9716–9725, 2021. [7](#)
- [12] Anatol Garioud, Nicolas Gonthier, Loic Landrieu, Apolline De Wit, Marion Valette, Marc Poupée, Sébastien Giordano, and boris Wattrelot. Flair : a country-scale land cover semantic segmentation dataset from multi-source optical imagery. In *Advances in Neural Information Processing Systems*, pages 16456–16482. Curran Associates, Inc., 2023. [4](#)
- [13] Anatol Garioud, Sébastien Giordano, Nicolas David, and Nicolas Gonthier. Flair-hub: Large-scale multimodal dataset for land cover and crop mapping, 2025. [1, 2, 4, 6, 3](#)
- [14] Shaohua Guo, Liang Liu, Zhenye Gan, Yabiao Wang, Wuhao Zhang, Chengjie Wang, Guannan Jiang, Wei Zhang, Ran Yi, Lizhuang Ma, and Ke Xu. Isdnet: Integrating shallow and deep networks for efficient ultra-high resolution segmentation. In *Proceedings of the IEEE/CVF Conference on Computer Vision and Pattern Recognition (CVPR)*, pages 4361–4370, 2022. [2, 3, 7](#)
- [15] Renlong Hang, Ping Yang, Feng Zhou, and Qingshan Liu. Multiscale progressive segmentation network for high-resolution remote sensing imagery. *IEEE Transactions on Geoscience and Remote Sensing*, 60:1–12, 2022. [2](#)
- [16] Kaiming He, Xiangyu Zhang, Shaoqing Ren, and Jian Sun. Deep residual learning for image recognition. In *Proceedings of the IEEE Conference on Computer Vision and Pattern Recognition (CVPR)*, 2016. [7](#)
- [17] Kaiming He, Xinlei Chen, Saining Xie, Yanghao Li, Piotr Dollár, and Ross Girshick. Masked autoencoders are scalable vision learners, 2021. [4](#)
- [18] Ziyan Huang, Haoyu Wang, Zhongying Deng, Jin Ye, Yanzhou Su, Hui Sun, Junjun He, Yun Gu, Lixu Gu, Shaoting Zhang, and Yu Qiao. Stu-net: Scalable and transferable medical image segmentation models empowered by large-scale supervised pre-training, 2023. [2](#)
- [19] Chuong Huynh, Anh Tuan Tran, Khoa Luu, and Minh Hoai. Progressive semantic segmentation. In *Proceedings of the IEEE/CVF Conference on Computer Vision and Pattern Recognition (CVPR)*, pages 16755–16764, 2021. [2](#)
- [20] Deyi Ji, Feng Zhao, and Hongtao Lu. Guided patch-grouping wavelet transformer with spatial congruence for ultra-high resolution segmentation, 2023. [1, 2](#)
- [21] Deyi Ji, Feng Zhao, Hongtao Lu, Mingyuan Tao, and Jieping Ye. Ultra-high resolution segmentation with ultra-rich context: A novel benchmark. In *Proceedings of the IEEE/CVF Conference on Computer Vision and Pattern Recognition (CVPR)*, pages 23621–23630, 2023. [1, 2, 4, 6, 7](#)
- [22] Yuyang Ji and Lianlei Shan. Ldnet: Semantic segmentation of high-resolution images via learnable patch proposal and dynamic refinement. In *2024 IEEE International Conference on Multimedia and Expo (ICME)*, pages 1–6, 2024. [2](#)
- [23] Antoine Labatie, Michael Vaccaro, Nina Lardiére, Anatol Garioud, and Nicolas Gonthier. Maestro: Masked autoencoders for multimodal, multitemporal, and multispectral earth observation data, 2025. [2, 6](#)

[24] Qi Li, Jiaxin Cai, Jiejin Luo, Yuanlong Yu, Jason Gu, Jia Pan, and Wenxi Liu. Memory-constrained semantic segmentation for ultra-high resolution uav imagery. *IEEE Robotics and Automation Letters*, 9(2):1708–1715, 2024. 2

[25] Hongyu Liu, Runmin Cong, Hua Li, Qianqian Xu, Qingming Huang, and Wei Zhang. ESNet: Evolution and succession network for high-resolution salient object detection. In *Forty-first International Conference on Machine Learning*, 2024. 3

[26] Wenshu Liu, Nan Cui, Luo Guo, Shihong Du, and Weiyin Wang. Desformer: A dual-branch encoding strategy for semantic segmentation of very-high-resolution remote sensing images based on feature interaction and multiscale context fusion. *IEEE Transactions on Geoscience and Remote Sensing*, 62:1–20, 2024. 2

[27] Yatong Liu, Yu Zhu, Ying Xin, Yanan Zhang, Dawei Yang, and Tao Xu. Mestrans: Multi-scale embedding spatial transformer for medical image segmentation. *Computer Methods and Programs in Biomedicine*, 233:107493, 2023. 2

[28] Ze Liu, Yutong Lin, Yue Cao, Han Hu, Yixuan Wei, Zheng Zhang, Stephen Lin, and Baining Guo. Swin transformer: Hierarchical vision transformer using shifted windows, 2021. 1, 2, 3

[29] Ze Liu, Han Hu, Yutong Lin, Zhiliang Yao, Zhenda Xie, Yixuan Wei, Jia Ning, Yue Cao, Zheng Zhang, Li Dong, Furu Wei, and Baining Guo. Swin transformer v2: Scaling up capacity and resolution. In *Proceedings of the IEEE/CVF Conference on Computer Vision and Pattern Recognition (CVPR)*, pages 12009–12019, 2022. 2

[30] Chen Lu, Xian Zhang, Kaile Du, Han Xu, and Guangcan Liu. Ctcfnet: Cnn-transformer complementary and fusion network for high-resolution remote sensing image semantic segmentation. *IEEE Transactions on Geoscience and Remote Sensing*, 62:1–17, 2024. 2

[31] Emmanuel Maggiori, Yuliya Tarabalka, Guillaume Charpiat, and Pierre Alliez. Can semantic labeling methods generalize to any city? the inria aerial image labeling benchmark. In *2017 IEEE International Geoscience and Remote Sensing Symposium (IGARSS)*, pages 3226–3229, 2017. 5

[32] Jishnu Mukhoti, Andreas Kirsch, Joost van Amersfoort, Philip H.S. Torr, and Yarin Gal. Deep deterministic uncertainty: A new simple baseline. In *Proceedings of the IEEE/CVF Conference on Computer Vision and Pattern Recognition (CVPR)*, pages 24384–24394, 2023. 3

[33] Qi, Lin Xindai, Yang Weixiang, He Shengfeng, Yu Yuanlong Liu Wenxi, and Li. Ultra-high resolution image segmentation via locality-aware context fusion and alternating local enhancement. *International Journal of Computer Vision*, 132:5030–5047, 2024. 2, 7

[34] Rong Qin, Xingyu Liu, Jinglei Shi, Liang Lin, and Jufeng Yang. Boosting the dual-stream architecture in ultra-high resolution segmentation with resolution-biased uncertainty estimation. In *Proceedings of the IEEE/CVF Conference on Computer Vision and Pattern Recognition (CVPR)*, pages 25960–25970, 2025. 1, 3, 5, 6, 7, 4

[35] Yanzhou Su, Jian Cheng, Haiwei Bai, Haijun Liu, and Changtao He. Semantic segmentation of very-high-resolution remote sensing images via deep multi-feature learning. *Remote Sensing*, 14, 2022. 2

[36] Yihao Sun, Mingrui Wang, Xiaoyi Huang, Chengshu Xin, and Yinan Sun. Fast semantic segmentation of ultra-high-resolution remote sensing images via score map and fast transformer-based fusion. *Remote Sensing*, 16(17), 2024. 2

[37] Loic Themyr, Clément Rambour, Nicolas Thome, Toby Collins, and Alexandre Hostettler. Full contextual attention for multi-resolution transformers in semantic segmentation. In *Proceedings of the IEEE/CVF Winter Conference on Applications of Computer Vision (WACV)*, pages 3224–3233, 2023. 2

[38] Matias Valdenegro-Toro. Sub-ensembles for fast uncertainty estimation in neural networks. In *Proceedings of the IEEE/CVF International Conference on Computer Vision (ICCV) Workshops*, pages 4119–4127, 2023. 3

[39] Hongzhen Wang, Ying Wang, Qian Zhang, Shiming Xiang, and Chunhong Pan. Gated convolutional neural network for semantic segmentation in high-resolution images. *Remote Sensing*, 9(5), 2017. 3

[40] Sai Wang, Yutian Lin, Yu Wu, and Bo Du. Toward real ultra image segmentation: Leveraging surrounding context to cultivate general segmentation model. In *Advances in Neural Information Processing Systems*, pages 129227–129249. Curran Associates, Inc., 2024. 2

[41] Wenhui Wang, Enze Xie, Xiang Li, Deng-Ping Fan, Kaitao Song, Ding Liang, Tong Lu, Ping Luo, and Ling Shao. Pyramid vision transformer: A versatile backbone for dense prediction without convolutions. In *Proceedings of the IEEE/CVF International Conference on Computer Vision (ICCV)*, pages 568–578, 2021. 2

[42] Wenhui Wang, Enze Xie, Xiang Li, Deng-Ping Fan, Kaitao Song, Ding Liang, Tong Lu, Ping Luo, and Ling Shao. Pvt v2: Improved baselines with pyramid vision transformer. *Computational Visual Media*, 8(3):415–424, 2022. 1, 2

[43] Honglin Wu, Peng Huang, Min Zhang, Wenlong Tang, and Xinyu Yu. Cmtfnet: Cnn and multiscale transformer fusion network for remote-sensing image semantic segmentation. *IEEE Transactions on Geoscience and Remote Sensing*, 61:1–12, 2023. 2

[44] Tong Wu, Zhenzhen Lei, Bingqian Lin, Cuihua Li, Yanyun Qu, and Yuan Xie. Patch proposal network for fast semantic segmentation of high-resolution images. *Proceedings of the AAAI Conference on Artificial Intelligence*, 34(07):12402–12409, 2020. 2, 3

[45] Tete Xiao, Yingcheng Liu, Bolei Zhou, Yuning Jiang, and Jian Sun. Unified perceptual parsing for scene understanding, 2018. 3

[46] Zhenda Xie, Zheng Zhang, Yue Cao, Yutong Lin, Jianmin Bao, Zhiliang Yao, Qi Dai, and Han Hu. Simmim: A simple framework for masked image modeling. In *Proceedings of the IEEE/CVF Conference on Computer Vision and Pattern Recognition (CVPR)*, pages 9653–9663, 2022. 1, 3, 4

[47] Fei Yang, Fenlong Jiang, Jianzhao Li, and Lei Lu. Mstrans: Multi-scale transformer for building extraction from hr remote sensing images. *Electronics*, 13, 2024. 2

[48] Zhan Zhang, Daoyu Shu, Guihe Gu, Wenkai Hu, Ru Wang, Xiaoling Chen, and Bingnan Yang. Ringformer-seg: A scalable and context-preserving vision transformer framework for semantic segmentation of ultra-high-resolution remote sensing imagery. *Remote Sensing*, 17:3064, 2025. [2](#)

# Context-Aware Semantic Segmentation via Stage-Wise Attention

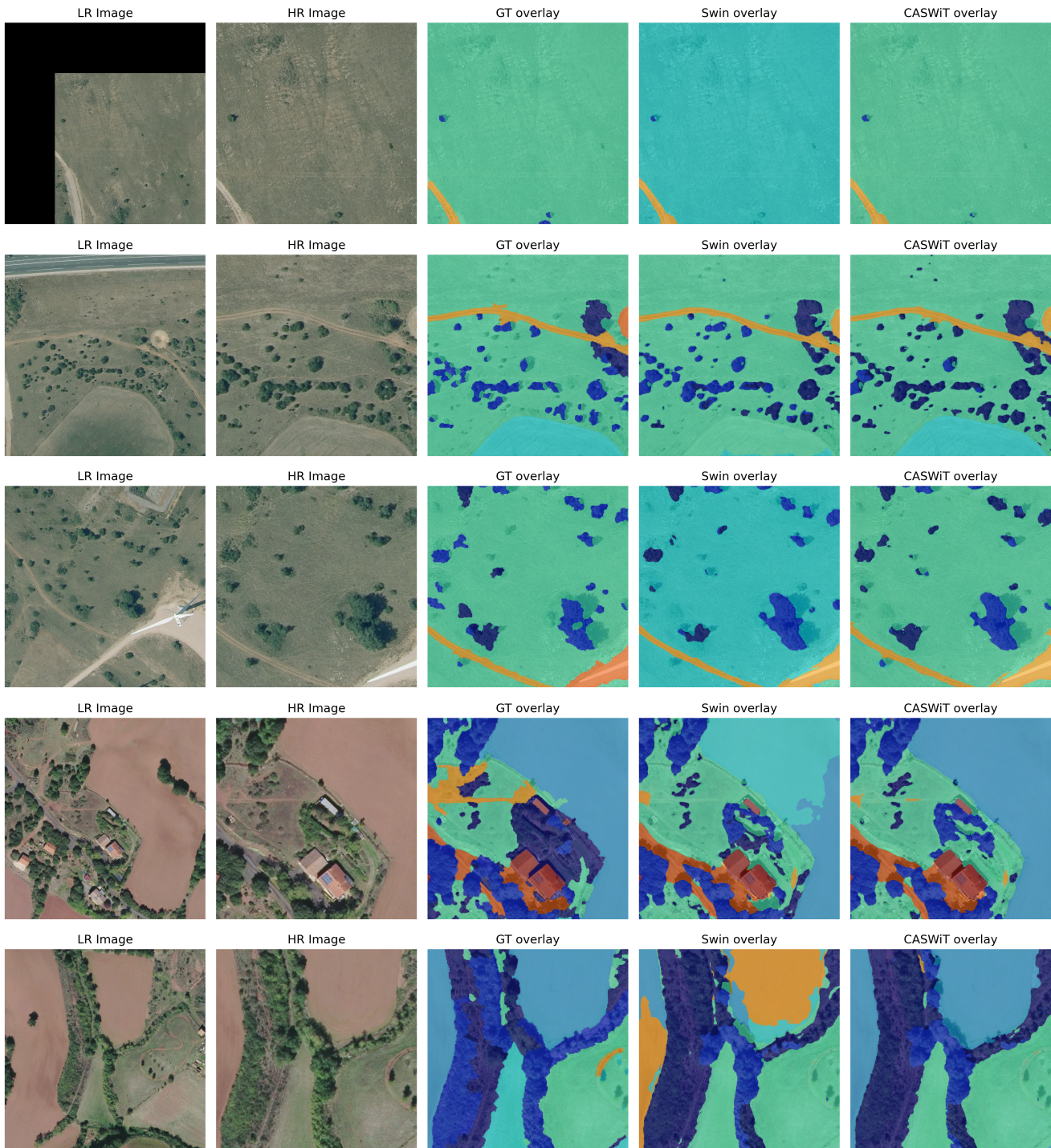
## Supplementary Material

### 7. URUR: illustrative annotation mismatch



Figure 7. Example where the provided mask (overlaid) locally diverges from the RGB content; such cases are occasional but can affect evaluation metrics. Visible classes include: **others**, **building**, **greenhouse**, **woodland**, **farmland**, **bareland**, **water**, **road**.

## 8. Qualitative analysis on FLAIR-HUB



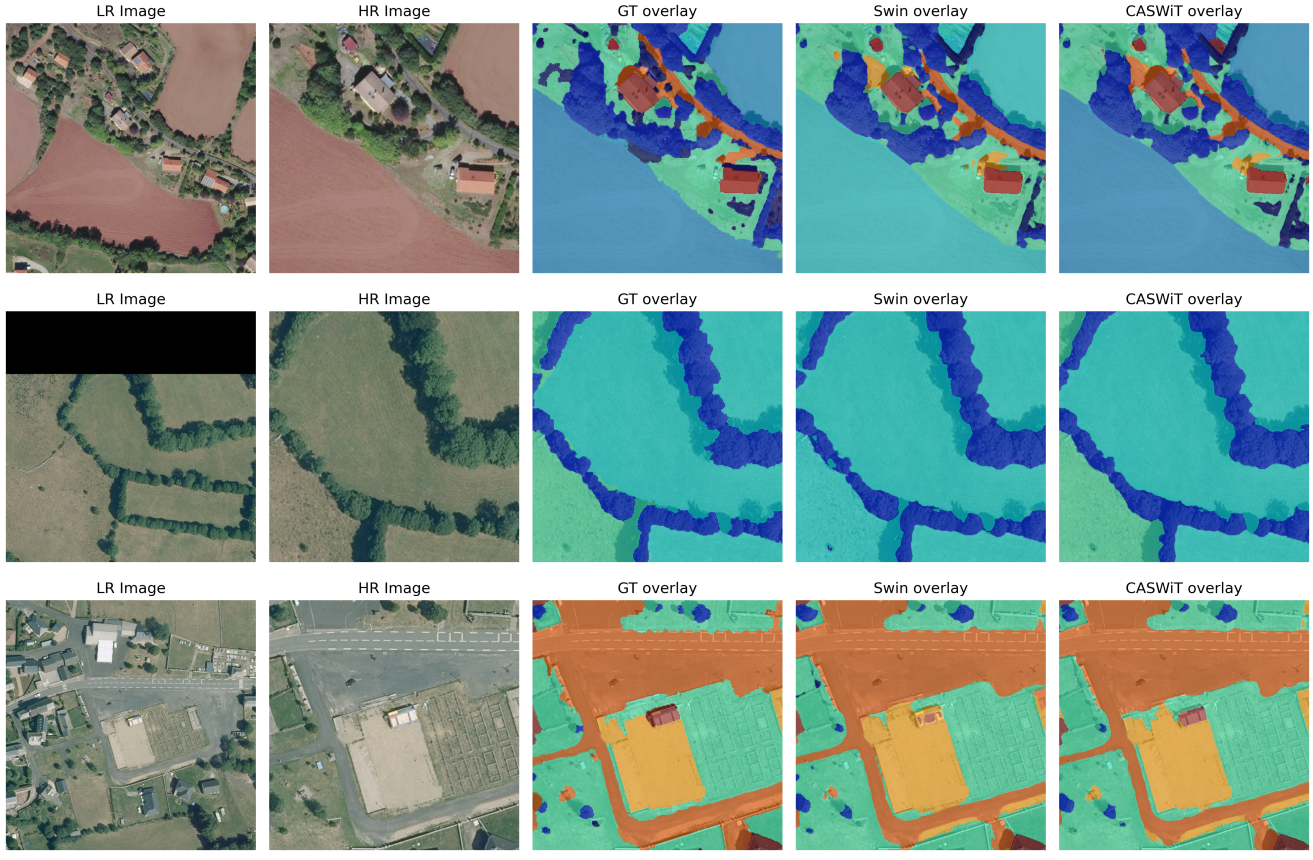


Figure 8. Comparison of LR/HR images, ground truth overlays, Swin Base predictions, and CASWiT predictions on eight test patches.

## 9. Supplementary results (IoUs)

Class	Swin-Base [13]	CASWiT-B (ours)	CASWiT-B-SSL (ours)	CASWiT-B-SSL-aug (ours)
Building	83.77	84.54	84.58	85.47
Greenhouse	77.89	78.87	78.61	79.46
Swimming pool	61.59	61.45	60.93	62.12
Impervious surface	75.03	76.24	76.48	76.78
Pervious surface	56.97	58.33	58.65	58.86
Bare soil	65.21	65.99	66.70	66.95
Water	90.08	89.37	90.26	90.65
Snow	67.77	70.21	67.84	66.59
Herbaceous vegetation	52.85	54.12	53.39	55.07
Agricultural land	56.53	57.58	59.34	60.38
Plowed land	37.34	38.40	39.99	38.20
Vineyard	78.88	79.29	80.51	80.71
Deciduous	70.07	70.68	71.31	71.47
Coniferous	58.95	59.93	61.11	62.89
Brushwood	30.97	31.68	30.55	31.79
mIoU	64.05	65.11	65.35	<b>65.83</b>

Table 4. Per-class IoU (%) on the FLAIRHUB RGB test set for Swin-Base and our CASWiT variants.

Class	WSDNET [21]	UHRS (Boosting dual branch) [34]	CASWiT-Base (ours)	CASWiT-Base-SSL (ours)
Others	-	-	0.00	0.00
Building	-	-	74.81	75.07
Farmland	-	-	79.16	79.19
Greenhouse	-	-	46.33	46.51
Woodland	-	-	51.61	52.10
Bareland	-	-	29.80	31.64
Water	-	-	56.36	54.90
Road	-	-	51.24	53.33
mIoU	46.9	48.2	48.7	<b>49.1</b>

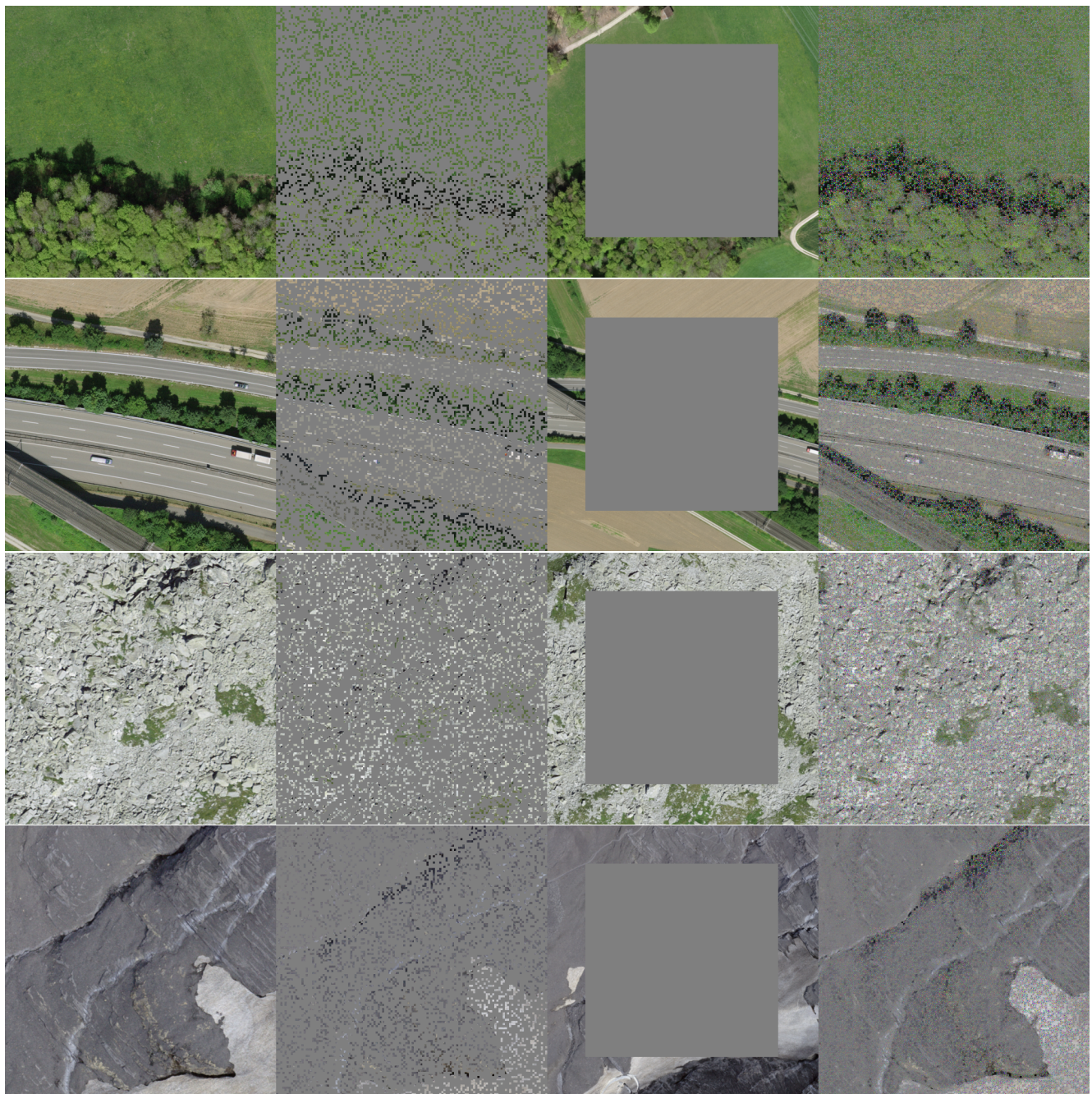
Table 5. Per-class IoU (%) on the URUR dataset test set for our CASWiT-Base models.

## 10. Dataset FLAIR-HUB merge



Figure 9. Examples of data pre-processing, on the left are the HR patches and on the right are the merged patches obtained from the available neighbors.

## 11. SSL results



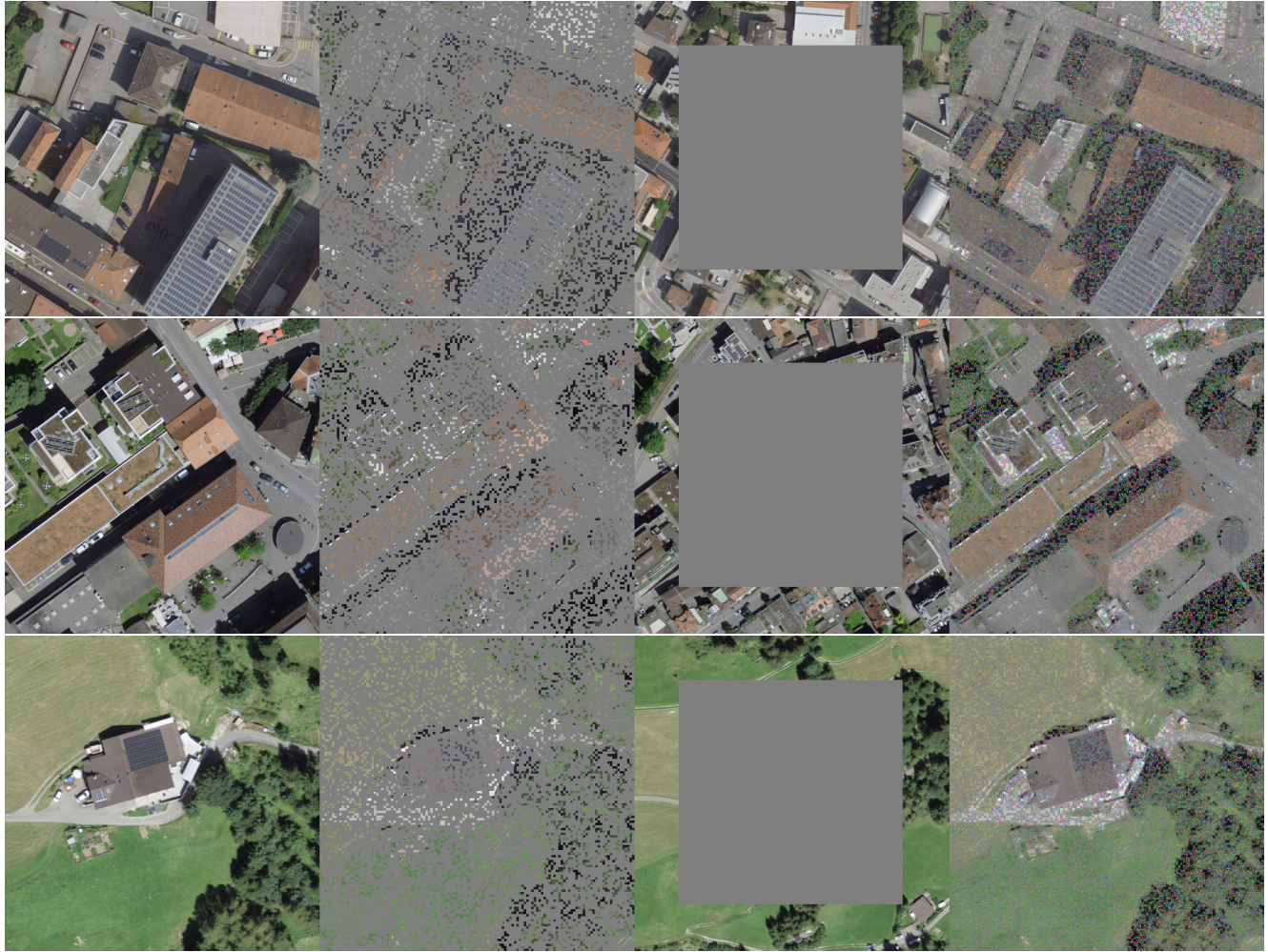


Figure 10. Self-supervised SimMIM-style inference results on the CASWiT-Base architecture. Each row (left to right) shows: original high-resolution image, high-resolution image with random masking, low-resolution image with central masking, and the reconstruction of the high-resolution image.

## 12. Cross-attention visualization

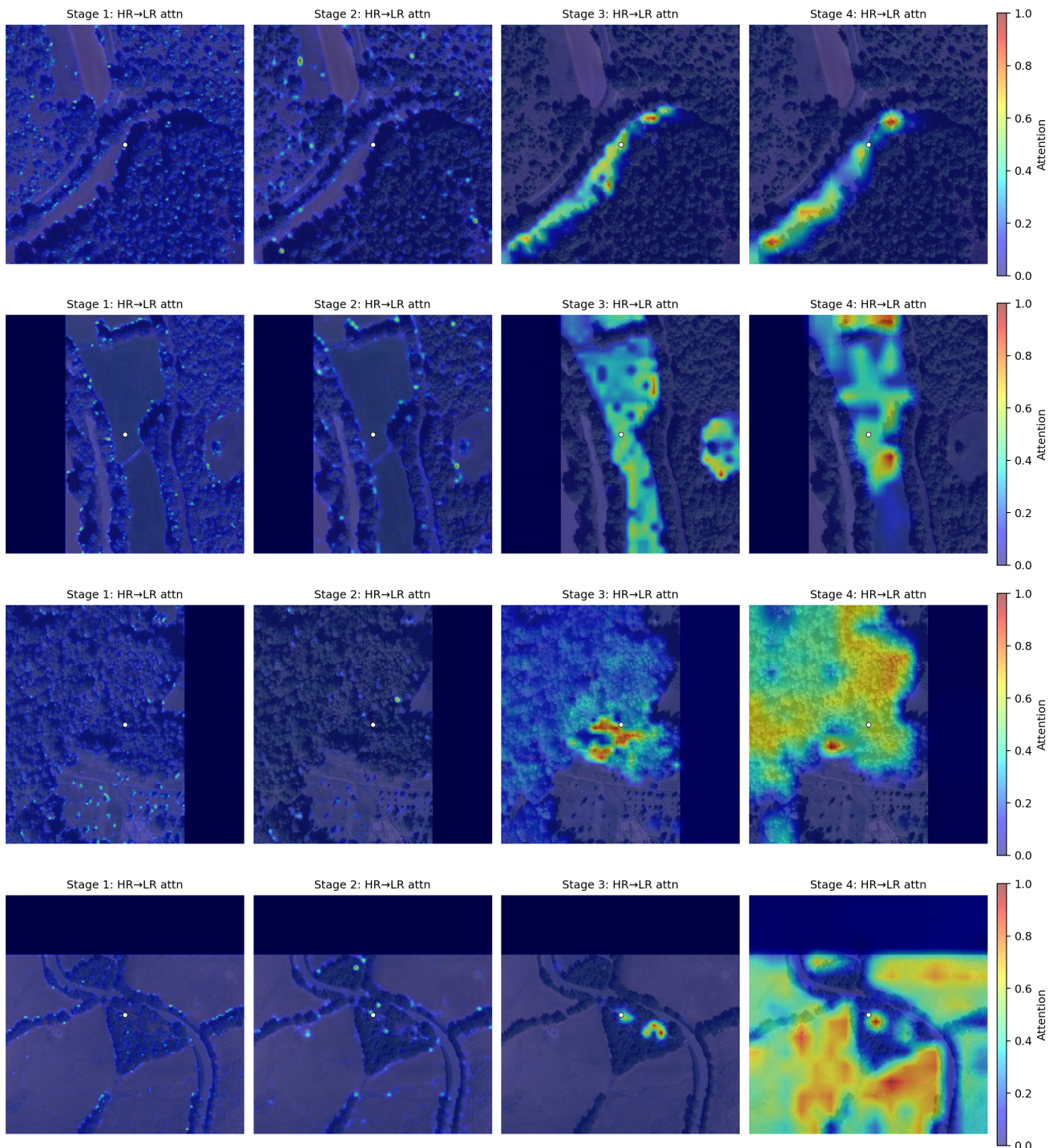


Figure 11. Visualization of cross-attention maps for each stage of the model on four test patches.